Monthly Notices
of the
ROYAL ASTRONOMICAL SOCIETY

MNRAS **436,** 3626–3639 (2013) doi:10.1093/mnras/stt1840
Advance Access publication 2013 October 24

Gamma-ray emission from massive stars interacting with active galactic nuclei jets

A. T. Araudo,[1]⋆ V. Bosch-Ramon[2] and G. E. Romero[3,4]

[1]*Centro de Radioastronomía y Astrofísica, Universidad Nacional Autónoma de México, A.P. 3-72 (Xangari), 58089 Morelia, Michoacán, Mexico*
[2]*Departament d'Astronomia i Meteorologia, Universitat de Barcelona, Martí i Franquès 1, E-08028 Barcelona, Spain*
[3]*Instituto Argentino de Radioastronomía, C.C.5, (1894) Villa Elisa, Buenos Aires, Argentina*
[4]*Facultad de Ciencias Astronómicas y Geofísicas, Universidad Nacional de La Plata, Paseo del Bosque, 1900 La Plata, Argentina*

Accepted 2013 September 26. Received 2013 September 26; in original form 2013 July 22

ABSTRACT

Dense populations of stars surround the nuclear regions of galaxies. In active galactic nuclei, these stars can interact with the relativistic jets launched by the supermassive black hole. In this work, we study the interaction of early-type stars with relativistic jets in active galactic nuclei. A bow-shaped double-shock structure is formed as a consequence of the interaction of the jet and the stellar wind of each early-type star. Particles can be accelerated up to relativistic energies in these shocks and emit high-energy radiation. We compute, considering different stellar densities of the galactic core, the gamma-ray emission produced by non-thermal radiative processes. This radiation may be significant in some cases, and its detection might yield valuable information on the properties of the stellar population in the galaxy nucleus, as well as on the relativistic jet. This emission is expected to be particularly relevant for nearby non-blazar sources.

Key words: radiation mechanisms: non-thermal – stars: early-type – galaxies: active – gamma-rays: theory.

1 INTRODUCTION

Active galactic nuclei (AGN) consist of a supermassive black hole (SMBH) surrounded by an accretion disc in the centre of a galaxy. Sometimes these objects present radio emitting jets originated close to the SMBH (Begelman, Blandford & Rees 1984). These jets may be very weak or absent in radio-quiet AGN, but in radio-loud sources bipolar powerful outflows of collimated plasma are ejected from the inner regions of the accretion disc.

Radio-loud AGN produce continuum radiation along the whole electromagnetic spectrum, from radio to gamma-rays. The thermal emission is radiated by matter heated during the accretion process (Shakura & Sunyaev 1973; Bisnovatyi-Kogan & Blinnikov 1977), whereas the non-thermal radiation is generated by relativistic particles accelerated in the jets (e.g. Böttcher 2007). This non-thermal emission is thought to be of synchrotron and inverse Compton (IC) origin (e.g. Ghisellini, Maraschi & Treves 1985), although hadronic models have been also considered to explain gamma-ray sources (e.g. Mannheim 1993; Mücke & Protheroe 2001; Aharonian 2002; Reynoso, Medina & Romero 2011; Romero & Reynoso 2011). In addition to continuum radiation, optical and ultraviolet emission lines are also produced in AGN. Some of these lines are broad, emitted by clumps of gas moving with velocities $v_g > 1000\,\mathrm{km\,s^{-1}}$ and located in a small region close to the SMBH, the so-called broad line region (BLR).

The presence of material surrounding the jets of AGN makes jet–medium interactions likely. For instance, the interaction of BLR clouds with AGN jets was already suggested by Blandford & Konigl (1979) as a mechanism for knot formation in the radio galaxy M87. Also, the gamma-ray production through the interaction of a cloud from the BLR with the jet was studied by Dar & Laor (1997), and more recently by Araudo, Bosch-Ramon & Romero (2010). In the latter work, the authors showed that jet–cloud interactions may generate detectable gamma-rays in non-blazar AGN, of transient nature in nearby low-luminous sources, and steady in the case of powerful objects.

In addition to clouds from the BLR, and also from the narrow line region (more extended and located further away from the nucleus), stars also surround the central region of AGN. Jet–star interactions have been historically studied as a possible mechanism of jet mass loading and deceleration in the past. In the seminal work of Komissarov (1994), the interaction of low-mass stars with jets was studied to analyse the mass transfer from the former to the latter in elliptical galaxies. Komissarov concluded that in low-luminous jets, the interaction with stars can significantly affect the jet dynamics and matter composition. In the same direction, Hubbard & Blackman (2006) analysed the mass loading and truncation of the jet by interactions with stars, also considering the case of an interposed stellar cluster.

⋆E-mail: a.araudo@crya.unam.mx

The gamma-ray emission generated by the interaction of massive stars with (blazar type) AGN jets has been studied by Bednarek & Protheroe (1997). They focused on the gamma-ray emission reprocessed by pair-Compton cascades in the radiation field of the star, and produced by relativistic electrons accelerated in the shocks formed by the interaction of the stellar wind with the jet. Recently, Barkov, Aharonian & Bosch-Ramon (2010) studied the interaction of red giant (RG) stars with AGN jets, focusing on the gamma-ray emission produced by the interaction between the tidally disrupted atmosphere of a RG with the inner jet (see also Barkov et al. 2012; Khangulyan et al. 2013).

In the present paper we adopt the main idea of Bednarek & Protheroe (1997), i.e. the interaction of massive stars with AGN jets, although our scenario consists of a population of massive stars surrounding the jets, and considers jet–star interactions at different heights (z) of the jet. We analyse the dependence with z of the properties of the interaction region (i.e. the shocks in the jet and the stellar wind), and also the subsequent non-thermal processes generated at these shocks. We consider the injection of relativistic electrons and protons, the evolution of these populations of particles by synchrotron and IC radiative processes in the case of leptons and proton–proton interactions for hadrons, as well as escape losses, and finally the production of X- and gamma-rays. We compute the radiation produced at different distances to the SMBH. In addition, we consider the particular case of a powerful Wolf–Rayet (WR) star interacting at 1 pc from the SMBH.

In the scenario considered here, the emitters are the flow downstream of the bow shocks located around the stars. This flow moves together with the stars at a non-relativistic speed, and thus the emission will not be relativistically boosted. For this reason the radiation from jet–star interactions will be mostly important in misaligned AGN, where the emission produced by other mechanisms in the jet (e.g. internal shocks; e.g. Rees 1978) is not amplified by Doppler boosting.[1]

Misaligned radio-loud AGN represent an increasing population of gamma-ray sources. The most populated energy band is the GeV region, in which *Fermi* has already detected at least 11 sources (Abdo et al. 2010), a population that is expected to grow in the near future. Because of this, theoretical models that can predict the level and spectrum of the gamma-ray emission from these sources are timely in order to contribute to the analysis and understanding of future detections. In this context, jet–massive star interactions are events that can produce detectable gamma-ray emission in AGN jets. This phenomenon may be important in spiral galaxies, where the star formation rate is high. In addition, some elliptical galaxies after a violent merger or collision processes (e.g. López-Sánchez 2010) are also expected to harbour a large number of massive stars near the active core. Finally, star formation may take place in the external regions of accretion discs of AGN (e.g. Hopkins & Quataert 2010), and thus a population of massive stars might exist in the galactic core of even typical elliptical hosts.

This paper is organized as follows. In Section 2 the main characteristics of the stellar population near the SMBH are presented. In Section 3, our model of jet–star interaction is described. In Sections 4 and 5, the acceleration of particles and the associated emission are studied. Then, in Sections 6 and 7, the emission produced by the interaction of a WR and a population of massive stars is calculated, and our main results are presented. Finally, a discussion is given in Section 8.

[1] We neglect emission produced in the shocked flows far from the star, where there might be boosting.

2 STELLAR POPULATIONS IN THE NUCLEUS OF GALAXIES

The characteristics of the stellar populations surrounding the SMBH in AGN depend on the type of host galaxy. Generally, in spiral galaxies the star formation rate $\dot{M}_\star$ is roughly constant, reaching values as large as $\sim$400 $\mathrm{M}_\odot\ \mathrm{yr}^{-1}$ (Mor et al. 2012), whereas elliptical galaxies contain large amounts of old stars and $\dot{M}_\star$ is very low. However, mergers between (elliptical) galaxies can lead to renewed nuclear activity and episodes of stellar formation (e.g. Sanders & Mirabel 1996), and accretion of matter to the SMBH may be associated with star formation in the galactic nuclei. In these cases $\dot{M}_\star \gtrsim 1000\ \mathrm{M}_\odot\ \mathrm{yr}^{-1}$ and the process is episodic.

The number of stars formed per mass (m), time (t) and volume ($V \propto r^3$) units can be expressed as $\psi(m, r, t) = \psi_0(m, r)\exp(-t/T)$ (Leitherer & Heckman 1995), where $\psi_0 \equiv \psi(t = 0)$, and t and T are the age of the stellar system and the duration of the formation process, respectively. There are two limit cases: continuous formation of stars ($t \ll T$) and starbursts ($t \gg T$). In the former case, t and T are the present age and the total lifetime of the host galaxy, respectively, and being $t \ll T$, ψ can be considered $\sim\psi_0$, and the assumption of a continuous and constant star formation process is reasonable. In the latter case, t and T are the age and duration of the burst, respectively, and all the stars are formed almost simultaneously, implying $\psi(t \gg T) \sim 0$. In the present work we consider that stellar formation processes take place continuously in the nuclear region of the galaxy, and the stars are uniformly distributed around the SMBH. The case of a jet interacting with a massive star-forming region will be considered separately in a future paper.

In the present work we assume that ψ is a power-law mass and radius distribution:

$$\psi = K \left(\frac{m}{\mathrm{M}_\odot}\right)^{-x} \left(\frac{r}{\mathrm{pc}}\right)^{-y}, \tag{1}$$

where $x \sim 2.3$ for the mass range $0.1 \leq m/\mathrm{M}_\odot \leq 120$ (Salpeter 1955; Kroupa 2001), y is a free parameter that we fix to 1, and 2, and $[K] = \mathrm{M}_\odot^{-1}\ \mathrm{yr}^{-1}\ \mathrm{pc}^{-3}$. Massive stars are formed in giant molecular clouds with mass $M_\mathrm{c} \sim 10^3$–$10^7\ \mathrm{M}_\odot$ and radius $R_\mathrm{c} \sim$ 10–200 pc. Stars are formed at a distance from the SMBH larger than the tidal radius:

$$r_\mathrm{t} \sim 2 \left(\frac{M_\mathrm{bh}}{10^7\ \mathrm{M}_\odot}\right)^{1/3} \left(\frac{M_\mathrm{c}}{10^3\ \mathrm{M}_\odot}\right)^{-1/3} \left(\frac{R_\mathrm{c}}{10\,\mathrm{pc}}\right)\ \mathrm{pc}, \tag{2}$$

with a star formation rate $\dot{M}_\star = \iint \psi\, m\, \mathrm{d}m\, \mathrm{d}V$, i.e.

$$\dot{M}_\star = K \int_{1\,\mathrm{pc}}^{1\,\mathrm{kpc}} \left(\frac{r}{\mathrm{pc}}\right)^{-y} 4\pi r^2\, \mathrm{d}r \int_{0.1\,\mathrm{M}_\odot}^{120\,\mathrm{M}_\odot} \left(\frac{m}{\mathrm{M}_\odot}\right)^{-x+1} \mathrm{d}m. \tag{3}$$

To obtain K, we consider the empirical relation obtained by Satyapal et al. (2005): $\dot{M}_\star = 47.86(\dot{M}_\mathrm{bh}/\mathrm{M}_\odot\ \mathrm{yr}^{-1})^{0.89}\ \mathrm{M}_\odot\ \mathrm{yr}^{-1}$, where $\dot{M}_\mathrm{bh}$ is the SMBH accretion rate. Considering that the accretion luminosity $L_\mathrm{accr} \sim 0.1\dot{M}_\mathrm{bh}c^2$ is a fraction η_accr of the Eddington luminosity, i.e. $L_\mathrm{accr} = \eta_\mathrm{accr}L_\mathrm{Edd}$, where $L_\mathrm{Edd} = 1.2 \times 10^{45}(M_\mathrm{bh}/10^7\ \mathrm{M}_\odot)\ \mathrm{erg\ s}^{-1}$ and M_bh is the mass of the SMBH, it is possible to write

$$\dot{M}_\star = 11.85\, \eta_\mathrm{accr}^{0.89} \left(\frac{M_\mathrm{bh}}{10^7\ \mathrm{M}_\odot}\right)^{0.89}\ \mathrm{M}_\odot\ \mathrm{yr}^{-1}. \tag{4}$$

Table 1. Different models considered in the present work. The label assigned to each model is constructed as $M_{\rm bh}$–$\eta_{\rm accr}$–$\eta_{\rm j}$. For instance, model M7-1-0.01 corresponds to a SMBH with mass $M_{\rm bh} = 10^7$ M$_\odot$ yr^{-1}, $\eta_{\rm accr} = 1$ and $\eta_{\rm j} = 0.01$.

$M_{\rm bh}$ (M$_\odot$)	z_0 (pc)	$L_{\rm Edd}$ (erg s^{-1})	$\eta_{\rm accr}$	$\dot{M}_\star$ (M$_\odot$ yr^{-1})	$\eta_{\rm j}$	$L_{\rm j}$ (erg s^{-1})	Model
10^7	5×10^{-5}	1.25×10^{45}	1	11.85	0.1	1.25×10^{44}	M7-1-0.1
					0.01	1.25×10^{43}	M7-1-0.01
					0.001	1.25×10^{42}	M7-1-0.001
			0.1	1.53	0.01	1.25×10^{43}	M7-0.1-0.01
					0.001	1.25×10^{42}	M7-0.1-0.001
			0.01	0.2	0.001	1.25×10^{42}	M7-0.1-0.001
10^8	5×10^{-4}	1.25×10^{46}	1	92.24	0.1	1.25×10^{45}	M8-1-0.1
					0.01	1.25×10^{44}	M8-1-0.01
					0.001	1.25×10^{43}	M8-1-0.001
			0.1	11.85	0.01	1.25×10^{44}	M8-0.1-0.01
					0.001	1.25×10^{43}	M8-0.1-0.001
			0.01	1.53	0.001	1.25×10^{43}	M8-0.1-0.001
10^9	5×10^{-3}	1.25×10^{47}	1	715.98	0.1	1.25×10^{46}	M9-1-0.1
					0.01	1.25×10^{45}	M9-1-0.01
					0.001	1.25×10^{44}	M9-1-0.001
			0.1	92.24	0.01	1.25×10^{45}	M9-0.1-0.01
					0.001	1.25×10^{44}	M9-0.1-0.001
			0.01	11.85	0.001	1.25×10^{44}	M9-0.1-0.001

In Table 1, $\dot{M}_\star$ is given for $M_{\rm bh} = 10^7$, 10^8 and 10^9 M$_\odot$, and $\eta_{\rm accr} = 0.01, 0.1$ and 1. Note that for the nine different combinations of $M_{\rm bh}$ and $\eta_{\rm accr}$, we obtain only five different values of $\dot{M}_\star$, from 0.2 to 716 M$_\odot$ yr^{-1}. Finally, equating equations (3) and (4), K results

$$K \sim \begin{cases} 3.22 \times 10^{-7}\, \eta_{\rm accr}^{0.89} \left(\frac{M_{\rm bh}}{10^7\,{\rm M}_\odot}\right)^{0.89}, & y = 1, \\ 1.6 \times 10^{-4}\, \eta_{\rm accr}^{0.89} \left(\frac{M_{\rm bh}}{10^7\,{\rm M}_\odot}\right)^{0.89}, & y = 2. \end{cases} \quad (5)$$

Once a stellar population is injected in the host galaxy, the new stars will evolve through collisions with other stars, mass loss by stellar evolution and by stellar disruption through the loss cone (this process will enlarge $M_{\rm BH}$). At the same time, stars migrate through the nuclear region forming a central cluster. Theoretical (e.g. Murphy, Cohn & Durisen 1991; Zhao 1997) and observational (e.g. Schödel, Merritt & Eckart 2009) studies show that stellar systems around a SMBH seem to follow a broken power-law spatial distribution $n_\star = n_{\rm b}(r/r_{\rm b})^{-y_{1,2}}$, where $n_{\rm b}$ is the number density at the break radius $r_{\rm b}$, and y_1 and y_2 are the power-law index inside and outside $r_{\rm b}$, respectively. The presence of a SMBH produces that the most massive stars are concentrated around it and, in some cases, a stellar cusp is formed very close to the event horizon, at $r \ll r_{\rm b}$, and with a slope ~ -0.5. This region is very small, but the density there is $\sim$10 times the density predicted by $n_\star = n_{\rm b}(r/r_{\rm b})^{-y_1}$ (Murphy et al. 1991; Zhao 1997). However, in systems with ongoing stellar formation, and low densities, relaxation time-scales as tidal disruption by the SMBH and collisions between stars can be neglected. Then, stars of a given mass are accumulated in the galaxy and, at a time $t < t_{\rm life}$, where $t_{\rm life} = a(m/{\rm M}_\odot)^{-b}$ is the stellar lifetime (in the main sequence), the density of stars is

$$n_{\star{\rm m}} = \int_0^t \psi(t')\,{\rm d}t' \approx \psi_0\, t \quad (6)$$

(Alexander 2005). For $t > t_{\rm life}$, stars die and the mass distribution becomes steeper than -2.3, following a law $n_{\star{\rm m}} \propto m^{-(2.3+b)}$. In the case of massive stars, $t_{\rm life} \sim (m/{\rm M}_\odot)^{-1.7}$ and $\sim$0.1 $(m/{\rm M}_\odot)^{-0.8}$ Gyr, for $7 < m/{\rm M}_\odot < 15$ and $15 < m/{\rm M}_\odot < 60$, respectively (Ekström et al. 2012). For $m > 60$ M$_\odot$, $t_{\rm life}$ is almost constant and around 0.004 Gyr (Crowther 2012). Then, at $t \gtrsim t_{\rm life}(8\,{\rm M}_\odot) \sim$ 0.03 Gyr, the rate of stellar formation is equal to the rate of stellar death and the system reaches the steady state for $m > 8\,{\rm M}_\odot$. In such a case, the number density of massive stars – $n_{\star{\rm M}}$ – keeps the spatial dependence of the stellar injection rate, $\psi \propto r^{-y}$, resulting

$$n_{\star{\rm M}} = \int_{8\,{\rm M}_\odot}^{120\,{\rm M}_\odot} n_{\star{\rm m}}\,{\rm d}m \sim 7.13 \times 10^5\, K \left(\frac{r}{\rm pc}\right)^{-y} {\rm pc}^{-3},$$

$$n_{\star{\rm M}} \sim \begin{cases} 0.23\, \eta_{\rm accr}^{0.89} \left(\frac{M_{\rm bh}}{10^7\,{\rm M}_\odot}\right)^{0.89} \left(\frac{r}{\rm pc}\right)^{-1}, & y = 1, \\ 114.14\, \eta_{\rm accr}^{0.89} \left(\frac{M_{\rm bh}}{10^7\,{\rm M}_\odot}\right)^{0.89} \left(\frac{r}{\rm pc}\right)^{-2}, & y = 2. \end{cases} \quad (7)$$

In Fig. 1, $n_{\star{\rm M}}$ is plotted for the different models described in Table 1, and for the cases of $y = 1$ and 2. We can see from the figures that at a distance $\sim$1 pc from the SMBH ($\sim 10^6 R_{\rm Schw} - R_{\rm Schw} = 2GM_{\rm bh}/c^2$ – for $M_{\rm bh} = 10^7$ M$_\odot$), the nominal density of stars is $\sim 10^4$ and 10 stars per pc^3 for the case of $y = 2$ and 1, respectively. This density decreases abruptly and at a distance $\sim$1 kpc from the centre the density of massive stars would be much less than one star per pc^3. Note that $n_{\star{\rm M}}$ depends on $\eta_{\rm accr} M_{\rm bh}$, and different combinations of $M_{\rm bh}$ and $\eta_{\rm accr}$ provide the same value of $n_{\star{\rm M}}$.

In the next section we calculate the number of massive stars that can enter the jet, which is related to the fraction of the volume occupied by stars that is intercepted by the jet of the AGN.

3 JET–STAR INTERACTION

We are interested in the study of the interactions between massive stars and jets in AGN. In this section, we describe the main characteristics of the interaction of a massive star with a relativistic jet.

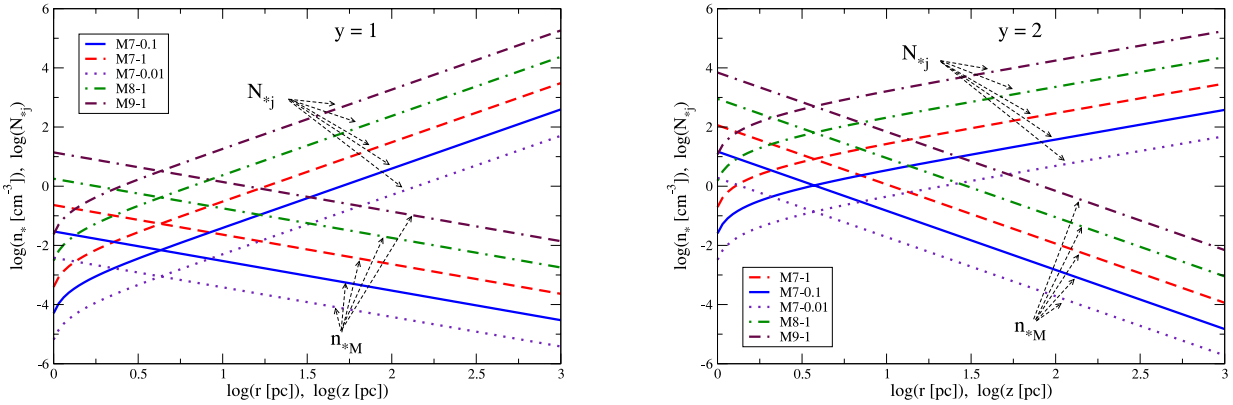

Figure 1. Density of massive stars ($n_{\star\mathrm{M}}$) and number ($N_{\star,\mathrm{j}}$) of early-type stars inside the jet at different values of z (that is equivalent to r), and for the case of $y = 1$ (left) and 2 (right). Cases for different combinations of M_{bh} and η_{accr} are plotted. Other combinations not shown in the figure provide the same $n_{\star\mathrm{M}}$ and $N_{\star\mathrm{j}}$ plotted here. In the legend box, we did not specify the value of η_{j} because the plotted magnitudes are independent of this parameter.

Jets of AGN are relativistic ($v_{\mathrm{j}} \sim c$), with macroscopic Lorentz factors $\Gamma \sim 5$–10. The matter composition of the jets is not well known because it depends on a yet incomplete jet formation theory. Two prescriptions are commonly adopted: a jet composed only by $e^{\pm}$ pairs (e.g. Komissarov 1994), and a lepto-hadronic jet (e.g. Reynoso et al. 2011), i.e. $n_{\mathrm{p}} = n_{\mathrm{e}}$, where n_{p} and n_{e} are the number density of protons and electrons, respectively. In such a case the jet density in the laboratory reference frame is $\rho_{\mathrm{j}} = \rho_{\mathrm{e}} + \rho_{\mathrm{p}} = \rho_{\mathrm{p}}[1 + (m_{\mathrm{e}}/m_{\mathrm{p}})] \sim \rho_{\mathrm{p}}$, being m_{e} and m_{p} the rest mass of electrons and protons, respectively. Thus, we determine the jet (number) density as $n_{\mathrm{j}} = \rho_{\mathrm{j}}/m_{\mathrm{p}} = L_{\mathrm{j}}/[(\Gamma - 1)m_{\mathrm{p}}c^2\sigma_{\mathrm{j}}v_{\mathrm{j}}]$, where L_{j} and $\sigma_{\mathrm{j}} = \pi R_{\mathrm{j}}^2$ are the jet kinetic luminosity and section, respectively, and R_{j} its radius. According to the current taxonomy of AGN, jets from type I Faranoff–Riley (FR I) galaxies are low luminous, with a kinetic luminosity $L_{\mathrm{j}} < 10^{44}$ erg s^{-1}, whereas FR II jets have $L_{\mathrm{j}} \gtrsim 10^{44}$ erg s^{-1}. The kinetic power of the jet is related with M_{bh} through the Eddington luminosity as $L_{\mathrm{j}} = \eta_{\mathrm{j}} L_{\mathrm{Edd}}$. In FR II sources, $\eta_{\mathrm{j}} \gtrsim 0.02$–0.7 (Ito et al. 2008), whereas in FR I, $\eta_{\mathrm{j}} \lesssim 0.01$. In the present work, we consider $\eta_{\mathrm{j}} < \eta_{\mathrm{accr}}$ (see Table 1). For the different models considered, L_{j} goes from 1.2×10^{42} to 1.2×10^{46} erg s^{-1}.

Jets are probably already formed at a distance $z_0 \sim 50\,R_{\mathrm{Schw}} \approx 5 \times 10^{-5}(M_{\mathrm{bh}}/10^7\,\mathrm{M}_{\odot})$ pc from the SMBH (e.g. Junor, Biretta & Livio 1999). The jet expands as $R_{\mathrm{j}} \sim z\tan\theta \sim \theta z$, where the half opening angle θ is $\sim 1^{\circ}$–10°. With this geometry, the number of massive stars contained inside the jet volume V_{j} is $N_{\star\mathrm{j}}(z) = \int_{1\,\mathrm{pc}}^{z} n_{\star\mathrm{M}}(z')\mathrm{d}V_{\mathrm{j}}$, where $\mathrm{d}V_{\mathrm{j}} = \pi R_{\mathrm{j}}^2 \mathrm{d}z'$ (z is the r-coordinate along the jet). This yields

$$N_{\star\mathrm{j}}(z) \sim \begin{cases} 2.89\,\eta_{\mathrm{accr}}^{0.89}\left(\frac{M_{\mathrm{bh}}}{10^7\,\mathrm{M}_{\odot}}\right)^{0.89}\left[\left(\frac{z}{\mathrm{pc}}\right)^2 - 1\right], & y = 1, \\ 1.43 \times 10^3\,\eta_{\mathrm{accr}}^{0.89}\left(\frac{M_{\mathrm{bh}}}{10^7\,\mathrm{M}_{\odot}}\right)^{0.89}\left[\left(\frac{z}{\mathrm{pc}}\right) - 1\right], & y = 2. \end{cases} \quad (8)$$

At $z \geq z_1 \sim 1.6\eta_{\mathrm{accr}}^{-0.89}(M_{\mathrm{bh}}/10^7\,\mathrm{M}_{\odot})^{-0.89}$ and $\eta_{\mathrm{accr}}^{-0.89}(M_{\mathrm{bh}}/10^7\,\mathrm{M}_{\odot})^{-0.89}$ pc, for the case of $y = 1$ and 2, respectively, there is at least one massive star inside the jet at every time (see Fig. 1). For z values such that $N_{\star\mathrm{j}} < 1$, then $N_{\star\mathrm{j}}$ is the fraction of time during which there is a star within the jet.

The permanence of stars inside the jet is determined by the jet crossing time $t_{\mathrm{j}} \sim 2R_{\mathrm{j}}/v_{\star} \sim 7 \times 10^2\,(z/\mathrm{pc})^{3/2}\,(M_{\mathrm{bh}}/10^7\,\mathrm{M}_{\odot})^{-1/2}$ yr, where $v_{\star} = (2GM_{\mathrm{bh}}/z)^{1/2} \sim 3 \times 10^7\,[(M_{\mathrm{bh}}/10^7\,\mathrm{M}_{\odot})(z/\mathrm{pc})]^{-1/2}$ cm s^{-1} is the velocity at which stars are moving around the SMBH.

Table 2. Jet and stellar parameters considered in this work.

Description	Value
Stellar mass distribution	$m = 8$–$120\,\mathrm{M}_{\odot}$
Stellar mass-loss rate	$\dot{M}_{\mathrm{w}} = 10^{-6}\,\mathrm{M}_{\odot}\,\mathrm{yr}^{-1}$
Stellar wind terminal velocity	$v_{\infty} = 2000\,\mathrm{km\,s}^{-1}$
Stellar luminosity	$L_{\star} = 3 \times 10^{38}\,\mathrm{erg\,s}^{-1}$
Surface temperature	$T_{\star} = 3 \times 10^4\,\mathrm{K}$
Stellar surface magnetic field	$B_{\mathrm{s}} = 10\,\mathrm{G}$
Accretion luminosity	$L_{\mathrm{accr}} = \eta_{\mathrm{accr}} L_{\mathrm{Edd}}$
Jet kinetic luminosity	$L_{\mathrm{j0}} = \eta_{\mathrm{j}} L_{\mathrm{Edd}}$
Jet velocity	$v_{\mathrm{j}} \approx c$
Jet Lorentz factor	$\Gamma_0 = 10$
Jet half opening angle	$\theta = 5^{\circ}$
Jet base	$z_0 = 50R_{\mathrm{Schw}}$

To analyse the interaction of stars with the jets, we need to know the structure of the shocks formed as a consequence of the collision of the jet plasma with the stellar wind. The double bow shock formed around the star (see Komissarov 1994 for a detailed study of the bow-shock structure and stability) depends not only on the jet properties, but also on the stellar ones, in particular the stellar wind mass-loss rate and velocity. Main-sequence massive (OB) stars have typically mass-loss rates $\dot{M}_{\mathrm{w}} \sim 10^{-7}$–$10^{-5}$ $\mathrm{M}_{\odot}$ yr^{-1}. This mass loss is radiatively driven, forming supersonic winds that reach terminal velocities $v_{\infty} \sim 3000\,\mathrm{km\,s}^{-1}$ in the fastest cases (e.g. Lamers & Cassinelli 1999). The luminosities and surface temperatures of OB stars are $L_{\star} \sim 10^{37}$–10^{39} erg s^{-1} and $T_{\star} \sim 3$–4×10^4 K, respectively, determining a stellar radius $R_{\star} = \sqrt{L_{\star}/(4\pi\sigma_{\mathrm{SB}}T_{\star}^4)} \sim 10\,\mathrm{R}_{\odot}(L_{\star}/3 \times 10^{38}\,\mathrm{erg\,s}^{-1})^{1/2}(T_{\star}/3 \times 10^4\,\mathrm{K})^{-2}$. Here $\sigma_{\mathrm{SB}} \sim 5.67 \times 10^{-5}$ erg cm^{-2} K^{-4} is the Stefan–Boltzmann constant. In the present work we fix the stellar and jet parameters to the values listed in Table 2.

3.1 The jet/stellar wind interaction

When the jet interacts with the wind of the star, a double bow shock is formed, as shown in Fig. 2. The stagnation point (SP) is located at a distance R_{sp} from the stellar centre, where the (shocked) wind and jet ram pressures are equal. From $\rho_{\mathrm{w}}\,v_{\mathrm{w}}^2 = \rho_{\mathrm{j}}\Gamma_0\beta_{\mathrm{j}}^2c^2$, where $\rho_{\mathrm{w}} = \dot{M}_{\mathrm{w}}/(4\pi R_{\mathrm{sp}}^2 v_{\mathrm{w}})$ and ρ_{j} are the wind and jet densities (in the laboratory reference frame), respectively. Equality of ram pressures

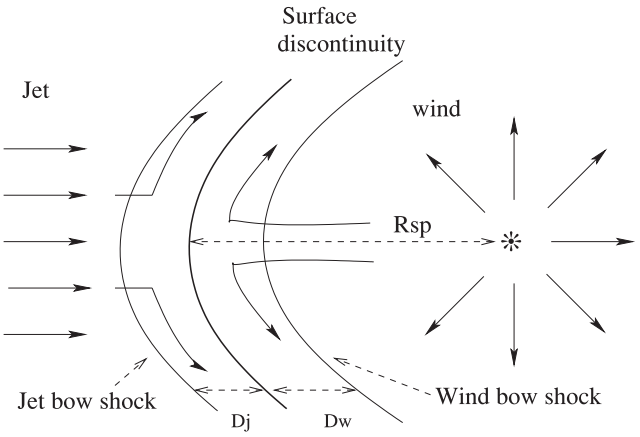

Figure 2. Sketch of the double bow-shock configuration formed by the interaction between the jet plasma and the stellar wind. Jet and wind shocked regions are separated by a contact discontinuity, and the shocked matter flows downstream, away from the shock apex. D_j and D_w are the size/thickness of the jet and wind bow-shock downstream regions.

yields

$$\frac{R_{sp,0}}{R_j} \sim 10^{-2} \left(\frac{\dot{M}_w}{10^{-6}\,M_\odot\,yr^{-1}}\right)^{1/2} \times \left(\frac{v_\infty}{2000\,km\,s^{-1}}\right)^{1/2} \left(\frac{L_{j0}}{10^{42}\,erg\,s^{-1}}\right)^{-1/2}, \quad (9)$$

where we have approximated the wind velocity v_w by $\sim v_\infty$.[2] Note that $R_{sp,0}$ depends on L_{j0}, and then only five combinations of the values of M_{bh} and η_j given in Table 1 provide different values of L_{j0} (and $R_{sp,0}$).

For the stellar parameters given in Table 2, R_{sp} will be larger than $R_\star$ at $z \geq z_{\star w} = 8\,(L_{j0}/10^{42}\,erg\,s^{-1})^{1/2}\,z_0$. Even if the stellar wind were very weak, the jet pressure might be still balanced by wind magnetic pressure. For a wind with a surface magnetic field $B_s = 10$ G, this can occur at $z \gtrsim z_{\star B} = 100\,z_0\,(B_s/10\,G)^{-1}(L_{j0}/10^{42}\,erg\,s^{-1})^{1/2}$; a magnetic field as high as 10^4 G would be required to balance the ram pressure of the jet near its base. At $z < z_\star \equiv \min\{z_{\star w}, z_{\star B}\}$, the jet flow will directly collide with the stellar surface and $R_{sp,0} \sim R_\star$. Either in the case the jet ram pressure is balanced by the magnetic field, or by the stellar surface, a shock can still form in the jet. On the other hand, no shock will form in the wind. Note that interactions at $z < z_\star$ will be very rare, since $z_\star < z_1$ for $0.014\eta_j^{0.5}\eta_{accr}^{0.89}(M_{bh}/10^7\,M_\odot)^{2.39} \lesssim 1$ for both values of y. (To obtain this limit we have considered that $z_\star = z_{\star w}$, because $z_\star = z_{\star B}$ only in cases with $B_s > 125$ G, which is not common in massive stars.)

The subscript 0 at L_j and R_{sp} in equation (9) refers the fact that jet/star interactions affect the jet power along z. The jet transfers a fraction $\sim(R_{sp}/R_j)^2$ of its kinetic energy to the bow shock that is formed around the star, and therefore L_j decreases with z. To evaluate this decrease of L_j caused by jet interactions with the stars, we adopt an exponential dilution factor of the jet kinetic luminosity:

[2] Considering that the wind velocity is described by a β law, i.e. $v_w = v_\infty(1 - R_\star/R)^\beta$, where $\beta \sim 0.8$–1, at distances $R \gtrsim 2R_\star$, the approximation $v_w \sim v_\infty$ is reasonable.

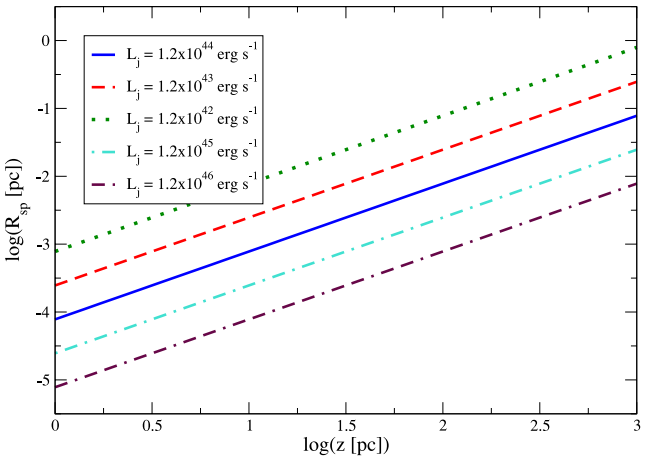

Figure 3. Location of the stagnation point R_{sp}. Five values of the jet kinetic luminosity have been considered: from $L_j = 1.2 \times 10^{42}$ to 1.2×10^{46} erg s^{-1} (see Table 1). Note that at $z \leq 1$ kpc, the exponential increase of R_{sp} is not present, given $R_{sp} \sim R_{sp,0}$.

$L_j(z) = L_{j0}\exp(-\tau)$, where τ accounts for the energy lost by all jet–star interactions up to z:

$$\tau(z) = \int_{z_0}^{z} \left(\frac{\sigma_{sp}}{\sigma_j}\right) n_\star(z')\,\sigma_j\,dz' = \int_{z_0}^{z} \pi R_{sp}^2\,n_{\star M}(z')\,dz', \quad (10)$$

where $\sigma_{sp} = \pi R_{sp}^2$ is the bow-shock section. Taking this into account, R_{sp} can be expressed with the following integral equation:

$$R_{sp} = R_{sp,0}(z)\exp\left[\int_{z_0}^{z} \frac{\pi}{2}\,n_{\star M}(z')\,R_{sp}^2(z')dz'\right], \quad (11)$$

whose solution is

$$R_{sp}(z) = \frac{R_{sp,0}}{\sqrt{1 - \left(\frac{R_{sp,0}}{z}\right)^2 \pi \int_{z_0}^{z} n_{\star M}(z')z'^2\,dz'}} = \frac{R_{sp,0}}{\sqrt{1 - \left(\frac{R_{sp,0}}{R_j}\right)^2 N_{\star j}(z)}}. \quad (12)$$

We have considered here only the impact of early-type stars because of the high power of their winds.

Fig. 3 shows the z dependence of R_{sp} for the different cases studied here. In particular, R_{sp} is plotted for different values of L_{j0}, from 1.2×10^{42} to 1.2×10^{46} erg s^{-1}, and adopting the parameters of jets and massive stars listed in Table 2. As shown in the figure, $R_{sp} \sim R_{sp,0}$ along the whole jet considered here (i.e. up to $z = 1$ kpc). For this reason, only the cases with different values of L_{j0} are plotted in Fig. 3. The value of z at which R_{sp} starts to be significantly larger than $R_{sp,0}$ is related to the condition $\tau > 1$. At $z < 1$ kpc, this condition is not fulfilled for any case considered here, as is shown in Fig. 3. Considering $R_{sp} = R_{sp,0}$ in equation (10), we obtain an upper limit on the value z_2 at which $\tau = 1$ (i.e. $(R_{sp,0}/R_j)^2\,N_{\star j}(z) = 1$). This yields

$$\frac{z_2}{kpc} \sim \begin{cases} 2\eta_j^{0.5}\eta_{accr}^{-0.45}(M_{bh}/10^7\,M_\odot)^{0.06}, & y = 1, \\ 8.4\eta_j\eta_{accr}^{-0.89}(M_{bh}/10^7\,M_\odot)^{0.11}, & y = 2. \end{cases} \quad (13)$$

Since we neglect flow re-acceleration downstream the bow shock, or shading of shocks by other shocks further upstream, when the energy rate crossing all the shocks reaches $\sim L_j$ (i.e. $\tau = 1$), the jet is completely stopped. When $\tau > 1$, the approximation of a constant

L_j is not valid any more. However, this occurs at $z > 1$ kpc on our models.

With the reduction of L_j by jet–star interactions, the jet velocity will decrease. For a cold jet $L_j = \dot{M}_j(\Gamma - 1)c^2$ and considering $\dot{M}_j$ constant, the Lorentz factor results $\Gamma = \Gamma_0 \exp(-\tau) + 1$. However, the assumption of constant $\dot{M}_j$ is not strictly correct. The entrainment of cold material from the stellar wind will also contribute to the deceleration of the jet bulk motion. In the surface discontinuity a mixing layer will develop, and the shocked jet and wind matter can mix. This mixing is produced by turbulent motions in the bow shock tail, likely triggered by Rayleigh–Taylor (RT) and Kelvin–Helmholtz (KH) instabilities. Under effective mixing, $\dot{M}_j(z) = \dot{M}_j^0 + \dot{M}_\star(z)$, where $\dot{M}_j^0$ is the initial rate of jet mass and $\dot{M}_\star(z) \sim N_{\star,j}(z)\,\dot{M}_w$. This effect has been analysed by Komissarov (1994) for the case of low-mass stars (typical $\dot{M}_w \sim 10^{-12}$ M$_\odot$ yr^{-1}) interacting with jets, concluding that mixing by KH instabilities is an important mechanism of mass loading in FR I galaxies. In the next subsection we show, through a simple analysis of time-scales, that KH instabilities are also important in the case of massive stars interacting with jets.

3.2 Dynamical time-scales

We are interested in the bow shocks generated around the stars as places for acceleration of particles and production of non-thermal emission. For this reason, even when we will not study the dynamics of these bow shocks, we will estimate the time during which stars can be inside the jet as obstacles, and the evolution and interplay of the shocked flows.

The time required by the star and its wind to penetrate into the jet is $t_p \sim 2R_{sp}/v_\star \sim 5.6 \times 10^2 (z/z_0)^{3/2}$ s. In addition to t_p and t_j, there are also hydrodynamical instabilities produced by the jet interaction that affect the shocked flows, triggering their disruption and mixing. The time-scale for full development of the two bow-shock structures is roughly $t_{bs} \sim R_{sp}/c_{sw}$, where c_{sw} is the sound speed in the wind shock, $c_{sw} \sim v_w$. This is also the time-scale on which RT and KH instabilities will lead to irregularities in the contact discontinuity of size $\sim R_{sp}$ (see e.g. Araudo, Bosch-Ramon & Romero 2009, and references therein, for a derivation of these time-scales); RT mainly acting in the region around the apex of the contact discontinuity, and KH in the outflowing tail, further downstream. For effective disruption of the two shocked flows, and their acceleration by the jet thrust and eventual mixing, a time of the order of few times t_{bs} is needed, which yields a length for the mixing tail of about few times $t_{bs}\, v_j \sim R_{sp}\, \chi^{1/2}$, where $\chi \equiv v_j/v_w \approx \sqrt{\rho_w/\Gamma\rho_j}$. If the ratio R_j/R_{sp} is of the order of or larger than χ, then jet dilution with z will not have a relevant impact on the process. Otherwise, jet dilution will likely weaken the instability growth on the largest tail scales, slowing down mixing. Effective mixing also requires that $t_{bs} < t_j$, since otherwise the interaction structure will not fully develop. Given the values of R_{sp}, R_j, $v_\star$ and v_w considered in this work, the mixing conditions seem to be fulfilled, and larger M_{bh} values (implying larger $v_\star$) should not have a significant impact. For simplicity, we have kept the reasoning at a basic level. For a more accurate and detailed description of tail disruption within relativistic jets, we refer to Blandford & Konigl (1979) and Komissarov (1994).

4 NON-THERMAL PARTICLES

In addition to the dynamical processes described above, non-thermal particles can be generated in jet–star interactions. In the bow shocks, particles can be accelerated up to relativistic energies through a Fermi-like type I acceleration mechanism. The size of the jet and wind shocked regions, D_j and D_w, respectively, is determined considering the conservation of the rate of the number particle density. Using relativistic and non-relativistic Rankine–Hugoniot relations[3] we obtain that $D_j \sim D_w \sim 0.3R_{sp}$.

Although the jet kinetic luminosity is much larger than the wind luminosity ($L_w = \dot{M}_w v_\infty^2/2$) at the location of R_{sp},

$$\frac{L_j}{L_w} = 5 \times 10^5 \left(\frac{L_j}{10^{42}\,\mathrm{erg\,s^{-1}}}\right)\left(\frac{\dot{M}_w}{10^{-6}\,\mathrm{M_\odot\,yr^{-1}}}\right)^{-1} \times \left(\frac{v_\infty}{2000\,\mathrm{km\,s^{-1}}}\right)^{-2}, \quad (14)$$

the available luminosity in the jet and wind bow shocks, L_{jbs} and L_{wbs}, respectively, is not so different: $L_{jbs}/L_{wbs} \sim 75\,(v_\infty/2000\,\mathrm{km\,s^{-1}})^{-1}$.

A fraction η_{nt} of these luminosities is transferred to particles accelerated in each shock, implying a non-thermal luminosity in the jet $L_{ntj} = \eta_{nt} L_{jbs}$, and in the wind $L_{ntw} = \eta_{nt} L_{wbs}$. The fraction η_{nt} is a free parameter of the present model. We assume that the populations of accelerated electrons and protons have the same luminosity, and we fix $\eta_{nt} = 0.1$ both in the jet and in the wind bow shocks. We note that the radiation luminosity scales simply as $\propto \eta_{nt}$.

Relativistic particles are assumed to be injected in the downstream region of the bow shocks following a power-law energy distribution: $Q_{e,p} \equiv K_{e,p}\, E_{e,p}^{-2.1}\, \exp(-E_{e,p}/E_{e,p}^{max})$, where $E_{e,p}^{max}$ is the maximum energy achieved by particles, and e and p stands for electrons and protons, respectively. A power-law index ~ -2 is usual for Fermi type I acceleration mechanisms, and the normalization constants $K_{e,p}$ are determined through $L_{nt} = \int Q_{e,p}\, E_{e,p}\, \mathrm{d}E_{e,p}$.

As a consequence of radiative and escape losses, the injected particles evolve until they reach the steady state, with characteristic time-scales $t_{adv,\,j} \sim 3R_{sp}/c$ and $t_{adv,\,w} \sim 4R_{sp}/v_\infty$, i.e. the advection escape times in the downstream regions of the jet and the wind bow shocks, respectively. In this work we consider that the emitting regions are uniform, i.e. we adopt a one-zone model for the accelerator/emitter. Under this condition, we solve the following equation to derive the energy distribution of relativistic electrons and protons, $N_{e,p}$ (Ginzburg & Syrovatskii 1964):

$$\frac{N_{e,p}}{t_{esc}} - \frac{\mathrm{d}}{\mathrm{d}E_{e,p}}(\dot{E}_{e,p} N_{e,p}) = Q_{e,p}, \quad (15)$$

where $t_{esc} = \min\{t_{adv},\, t_{diff}\}$. The diffusion time-scale is $t_{diff} \sim D_{j,w}^2 q\, B_{jbs,wbs}/(E_{e,p}\, c)$ in the Bohm regime, where B_{jbs} and B_{wbs} are the magnetic fields in the jet and the stellar wind bow-shock regions, respectively, and q is the electron charge. In addition to diffusion, particles suffer different relevant radiative losses $\dot{E}_{e,p}$, synchrotron and stellar photon IC upscattering for electrons, and proton–proton (Kelner, Aharonian & Bugayov 2006). All mentioned losses balance the energy gain from acceleration, $\dot{E}_{e,p}^{acc}$, when the steady state is achieved.

4.1 Particle acceleration and losses in the jet shock

The fraction of the jet section that is intercepted by the stellar bow shock, $\eta_j = \sigma_{sp}/\sigma_j$, is $\propto L_j^{-1}$. Therefore, $L_{jbs} = \eta_j L_j$ results to be

[3] We have considered the Rankine–Hugoniot relations obtained for the case of a plane shock.

independent of L_j and z:

$$L_{jbs} = \left(\frac{R_{sp}}{R_j}\right)^2 L_j \sim 10^{38} \left(\frac{\dot{M}_w}{10^{-6}\,M_\odot\,yr^{-1}}\right)\left(\frac{v_\infty}{2000\,km\,s^{-1}}\right) erg\,s^{-1}. \quad (16)$$

Note however that for rare cases of stars interacting at $z < z_\star$, $R_{sp} = R_\star$ and L_{jbs} is $\propto L_j\, z^{-2}$. The jet bow shock has a velocity $\sim v_j$, and particles are accelerated at this relativistic shock with a rate assumed to be $\dot{E}^{acc}_{e,p} \sim 0.01 q\, B_{jbs} c$. We adopt a modest acceleration efficiency, although for relativistic shocks, values as high as $\dot{E}^{acc}_{e,p} \sim 0.1 q\, B_{jbs} c$ have been derived (e.g. Achterberg et al. 2001).

Theoretical studies on jet acceleration (e.g. Komissarov et al. 2007) suggest that near the base of the outflow, the kinetic energy density of the jet, $U_{kin} = L_j/(\sigma_j v_j)$, is smaller than the magnetic energy density $U_{mag} = B_j^2/8\pi$, where B_j is the jet magnetic field. However, at $z \gtrsim 10^{-3}(M_{bh}/10^7\,M_\odot)(\theta/5^\circ)^{-1}$ pc, magnetic forces have already accelerated the flow and U_{kin} is likely to be dominant. Given that we are interested on the jet properties at $z \geq 1$ pc, we estimate B_j assuming that $U_{mag} = \eta_B U_{kin}$, with $\eta_B = 0.3$ (see fig. 8 of Komissarov et al. 2007 for the case of conical jets). The corresponding magnetic field is

$$B_j \sim 0.34 \left(\frac{\eta_B}{0.3}\right)^{1/2}\left(\frac{L_j}{10^{42}\,erg\,s^{-1}}\right)^{1/2}\left(\frac{\theta}{5^\circ}\right)^{-1}\left(\frac{z}{pc}\right)^{-1} G. \quad (17)$$

Then, assuming that in the bow shock downstream region is amplified by the compression of the flow, B_{jbs} results $\sim 4B_j \sim 1.4[(\eta_B/0.3)(L_j/10^{42}\,erg\,s^{-1})]^{1/2}(z/pc)^{-1}$ G.

The most important radiative losses of relativistic electrons in the jet bow-shock region are synchrotron and IC scattering of photons from the star. At R_{sp}, the energy density of photons is $U_\star \approx L_\star/(4\pi R_{sp}^2\, c) \sim (L_j/10^{42}\,erg\,s^{-1})(z/pc)^{-2}$ erg cm^{-3}. Considering that these photons follow a thermal distribution with a maximum at an energy $E_0 \approx 3K_B T_\star \sim 10(T_\star/3 \times 10^4\,K)$ eV ($K_B = 1.4 \times 10^{-16}$ erg K^{-1} is the Boltzmann constant), at $E_e > (m_e c^2)^2/E_0 \sim 50$ GeV, the IC interaction occurs in the Klein–Nishina (KN) regime. Photons from the accretion disc are a less important target for IC interactions compared with photons from the star, as seen from the large value of the ratio $U_\star/U_d \sim 10^2$, for the wind parameters adopted here and adopting a disc luminosity $\sim L_j$. Electrons can also radiate through relativistic Bremsstrahlung in interactions with the shocked jet matter. Nevertheless, densities are so low that relativistic Bremsstrahlung losses are quite inefficient when compared with escape, synchrotron or IC scattering.

The maximum energy achieved by electrons in the jet shock is determined by synchrotron losses resulting

$$\frac{E_e^{max}}{TeV} \sim 20.3 \left(\frac{\eta_B}{0.03}\right)^{-1/4}\left(\frac{z}{pc}\right)^{1/2}\left(\frac{L_j}{10^{42}\,erg\,s^{-1}}\right)^{-1/4}. \quad (18)$$

In Fig. 4, E_e^{max} is plotted for different values of L_j. Taking into account the escape, synchrotron and IC losses described above, we solve equation (15) obtaining the energy distribution N_e of relativistic electrons shown in Fig. 5 (left). The synchrotron and IC cooling dominate the high-energy part of the electron energy distribution, and at low energies advective losses are dominant. This appears as a steepening in N_e from $\propto E^{-2.1}$ to $\propto E^{-3.1}$.

The maximum energy of protons accelerated in the jet shock is determined by advection losses, giving $E_p^{max} \sim 2 \times 10^4 (\eta_B/0.03)^{-1/2}$ TeV. These relativistic protons escape from the jet bow-shock region advected by shocked matter, without producing significant levels of radiation. For this reason we do not take into account hadronic emission from the jet shocked region. Given that the proton energy is below the photomeson production threshold with stellar photons as targets, this process can also be neglected.

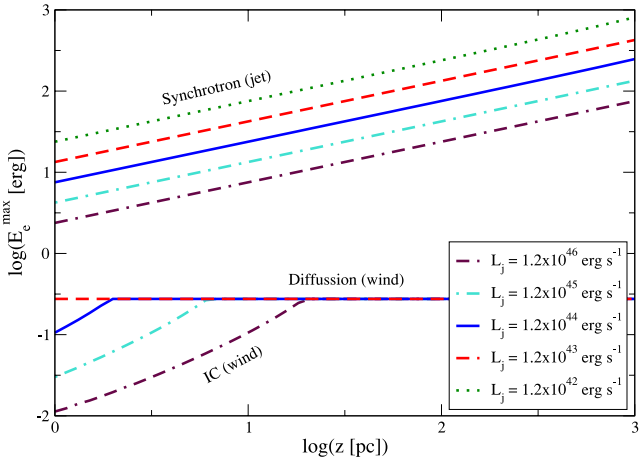

Figure 4. Maximum energies of electrons accelerated in the jet (top) and wind (bottom) bow shocks at different z, and for jet kinetic luminosities from $L_j = 1.2 \times 10^{42}$ to 1.2×10^{46} erg s^{-1}.

4.2 Particle acceleration and losses in the wind shock

Assuming that the whole wind is shocked, the shock luminosity would be

$$L_{wbs} \approx 1.3 \times 10^{36} \left(\frac{\dot{M}_w}{10^{-6}\,M_\odot\,yr^{-1}}\right)\left(\frac{v_\infty}{2000\,km\,s^{-1}}\right)^2 erg\,s^{-1}. \quad (19)$$

Being this shock non-relativistic, with velocity $\sim v_\infty$, particles are accelerated with a rate $\dot{E}^{acc}_{e,p} = (1/2\pi)\, q\, (v_\infty/c)^2\, B_w c$ (e.g. Drury 1983).

The magnetic field of the wind, B_w, roughly has a dipolar structure close to the star surface, and radial and toroidal components dominate farther out (Usov & Melrose 1992). For simplicity, we will adopt here $B_{wbs} \sim B_w$. Fixing $B_s = 10$ G, B_{wbs} results $\sim 0.1 B_{jbs}$ at $z > z_\star$, and synchrotron cooling will be more efficient in the jet than in the wind shocked region. On the other hand, given that the size and radiation field values are similar, the IC cooling time-scale in the wind shocked region is similar to the one in the jet. The main difference is in the advection time-scale and the maximum energy, given the much lower shock velocity. The lower advection speed implies that the electron energy distribution steepens at lower energies, implying a high radiation efficiency. The maximum energy of electrons accelerated in the wind is determined by IC and diffusion losses, providing the values of E_e^{max} plotted in Fig. 4.[4] The lower maximum energy, for the same non-thermal fraction, also increases the normalization of the energy distribution. Therefore, although the energetics of the wind shock is $\sim$100 times smaller than that in the jet shock, the contribution of accelerated electrons in the former to the non-thermal output may be significant. The resulting N_e is shown in Fig. 5 (right), and it is similar to the distribution of electrons accelerated in the jet, i.e. at low values of z N_e is $\propto E_e^{-3.1}$

[4] We cannot provide an analytical expression for E_e^{max} in the wind because in the range where it is constrained by IC scattering in the KN regime, the calculation was done through the Runge–Kutta numerical method.

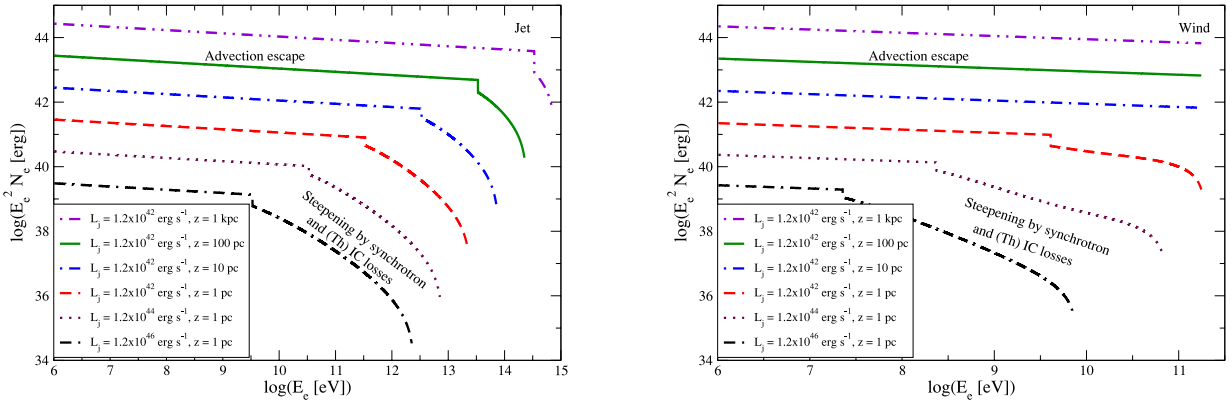

Figure 5. SED of electrons accelerated in the jet (left) and in the wind (right) bow shock at $z = 1$, 10, 100 and 10^4 pc), for $L_j = 1.2 \times 10^{42}$, 1.2×10^{44} and 1.2×10^{46} erg s^{-1}. The cases with $L_j = 1.2 \times 10^{44}$ erg s^{-1} at $z = 10$, 100 and 10^4 pc are equal to the cases with $L_j = 1.2 \times 10^{42}$ erg s^{-1} at $z = 1$, 10 and 100 pc, respectively. Also, the cases with $L_j = 1.2 \times 10^{46}$ erg s^{-1} at $z = 10$, 100 and 10^4 pc are equal to the cases with $L_j = 1.2 \times 10^{44}$ erg s^{-1} at $z = 1$, 10, and 100 pc, respectively.

as a consequence of IC and synchrotron losses, with a hardening beyond ∼10 GeV. At larger heights, $N_e \propto E_e^{-2.1}$ all the way up to E_e^{max} as a consequence of advection escape losses.

Regarding protons, the large wind particle densities imply that the proton–proton cooling channel is more efficient than in the jet shocked region, but still it is a minor channel of gamma-ray production compared with IC for the same e and p energetics. The proton energy distribution is dominated by advection losses, which are independent of energy, and therefore it keeps the injection slope, i.e. $N_p \propto E_p^{-2}$. The maximum energy of protons is constrained by diffusion losses, giving $E_p^{max} = 0.2(B_s/10\,\mathrm{G})(v_w/2000\,\mathrm{km\,s^{-1}})$ TeV.

5 NON-THERMAL EMISSION

Once N_e in the jet and wind shocked regions is computed, we calculate the spectral energy distribution (SED) of the non-thermal radiation, synchrotron and IC scattering (in Thomson and KN regimes) in the jet and the wind shocked regions, using the standard formulae (e.g. Blumenthal & Gould 1970). The energy budget for the emission produced in the bow shock regions is $\eta_{nt}L_{jbs}$ and $\eta_{nt}L_{wbs}$, which would be an upper limit for the emission luminosity produced both in the jet and in the wind, respectively.

An important characteristic of the scenario studied in this paper is that the emitter is fixed to the star, and being the star moving at a non-relativistic velocity, the emission produced in the bow shock regions is not amplified by Doppler boosting.

At radio wavelengths, the synchrotron self-absorption effect has been taken into account, although it is only relevant for interactions very close to the jet base. At gamma-ray energies, photon–photon absorption due to the presence of the stellar radiation field can be relevant at certain z (e.g. Bednarek & Protheroe 1997), but the internal absorption due to synchrotron radiation is negligible. Given the typical stellar photon energy $E_0 \sim 10$ eV, gamma-rays beyond ∼30 GeV can be affected by photon–photon absorption. However, this process is only important at small z, where R_{sp} is also small. At $z > 1$ pc SEDs shown in Fig. 6 are not strongly absorbed. Another effect that should be taken into account at energies beyond 100 GeV is absorption in the extragalactic background light via pair creation (important only for sources located well beyond 100 Mpc).

The leptonic emission is indistinguishable if R_{sp} is the same, regardless the z of interaction and L_j. However, more powerful jets have a transition from radiation to advection-dominated interactions at higher z values, which enhances their non-thermal luminosity. Synchrotron and IC losses are proportional to magnetic (energy) and radiation densities, and thus are $\propto z^{-2}$. The increase of the time during which particles remain in the emitter, $\propto z$, and the growth of the number of stars within a jet slice, $\propto z^{0.25}$, are not enough to balance the loss in radiation efficiency beyond the z at which radiation cooling is not dominant (at any particle energy). This implies that there is more emission generated at relatively small z values. To illustrate the changes in the SED with z, we present in Fig. 6 the synchrotron and IC emission produced by the interaction of only one star with the jet at $z = 1$, 10, 100 and 10^4 pc, an adopting the parameters listed in Table 2 for the different models presented in Table 1. (A detailed description of Fig. 6 is given in Sections 5.1 and 5.2.) In addition to that, we calculate the bolometric luminosities achieved by synchrotron and IC emission in the jet – L_z^j – and in the wind – L_z^w – by the interaction of only one star at different z: from 1 pc to 1 kpc. In Fig. 7, L_z^j and L_z^w (maroon solid lines) are shown. (A detailed description of this figure is given in Sections 5.1 and 5.2, and also in Section 7.)

5.1 Leptonic emission from the jet shock

The synchrotron and IC emission from the jet bow shock are presented in Fig. 6 (left-hand panel). As mentioned, both synchrotron and IC are more efficient in the inner jet regions, emission at lower energies getting less efficient (due to advection) at higher z values. This effect is clearly seen in Figs 6 and 7 (both in the left-hand panel).

In Fig. 6 we see different spectral features in the cases of $L_j = 1.2 \times 10^{42}$ (top) and 1.2×10^{46} erg s^{-1} (bottom). In the former case, the break energy in the photon spectrum is higher than in the latter case. This is very clear in the synchrotron emission, where the break energy in the case of $L_j = 1.2 \times 10^{42}$ erg s^{-1} is about 10^3 times larger than in the case of $L_j = 1.2 \times 10^{46}$ erg s^{-1}. (Compare Figs 6 and 5.) Another clear difference is the break produced by synchrotron self-absorption, being the source optically thin at lower energies in the case of $L_j = 1.2 \times 10^{42}$ erg s^{-1} than in the case of $L_j = 1.2 \times 10^{46}$ erg s^{-1}. Photon–photon absorption in the IC spectrum is not relevant in any case.

The total bolometric luminosity produced in the jet, $L_z^j = L_{IC,z}^j + L_{synchr,z}^j$, where $L_{IC,z}^j$ and $L_{synchr,z}^j$ are the bolometric luminosities of IC and synchrotron radiation in the jet, respectively, is plotted

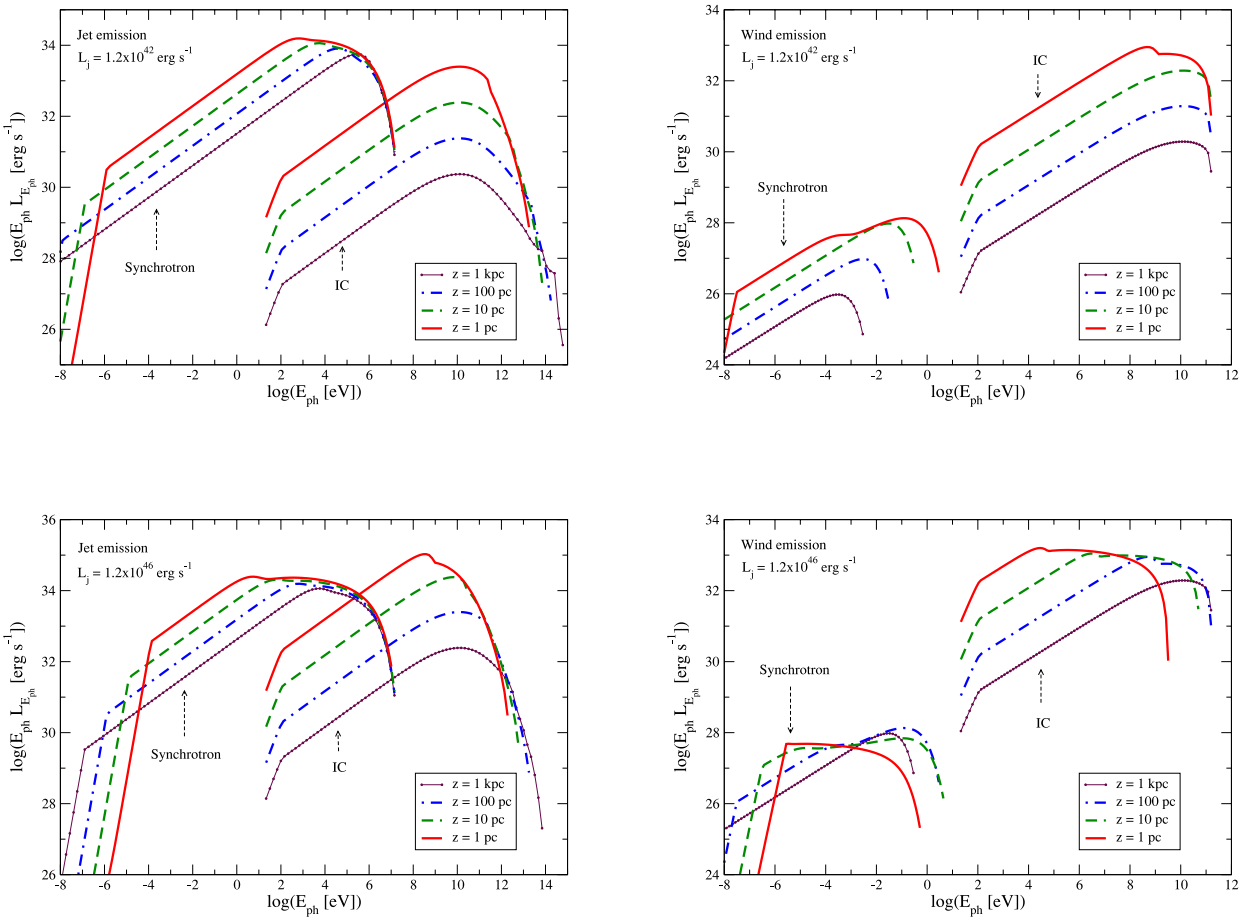

Figure 6. SED produced by the interaction of only one massive star with a jet of $L_{\rm j} = 1.2 \times 10^{42}$ (top) and 1.2×10^{46} erg s^{-1} (bottom) at $z = 1$ (red solid lines), 10 (green dashed lines), 100 (blue dot–dashed lines) and 10^4 pc (maroon dotted lines). The emission produced in the jet and in the wind is shown in the left- and right-hand panels, respectively.

in the left-hand panel of Fig. 7 (maroon solid line). Note that at $z \geq 1$ pc, where $R_{\rm sp} \propto z$, $L_{\rm ntj} \sim 10^{37}$ erg s^{-1} is constant on z as is shown in Fig. 7 with a black solid line.

5.2 Leptonic emission from the wind shock

The synchrotron and IC emission from the wind bow shock are presented in Fig. 6 (right-hand panel), also for the cases of only one star interacting with a jet of $L_{\rm j} = 1.2 \times 10^{42}$ (top) and 1.2×10^{46} erg s^{-1} (bottom), at $z = 1$, 10, 100 and 10^4 pc. The SED shows lower maximum energies and lower achieved emission levels than those of the shocked jet region. We can see from the figure that the synchrotron emission produced in the wind is very faint, with a specific luminosity about five order of magnitude lower than the IC emission.

The total bolometric luminosity produced in the wind, $L_z^{\rm w} = L_{{\rm IC},z}^{\rm w} + L_{{\rm synchr},z}^{\rm w} \sim L_{{\rm IC},z}^{\rm w}$, is plotted in the right-hand panel of Fig. 7 (maroon solid line). Note that at $z \geq 1$ pc, $L_z^{\rm w} \propto z^{-1}$. Finally, note that as a consequence of $t_{\rm adv}^{\rm w}/t_{\rm adv}^{\rm j} \sim 100$, because $v_\infty/c \sim 100$, the fraction of the available non-thermal luminosity that is radiated in the wind is larger than in the case of the jet emission, i.e. $L_z^{\rm w}/L_{\rm ntw} > L_z^{\rm j}/L_{\rm ntj}$.

Although $n_{\rm w}$ is larger than in the shocked jet region, the production of gamma-rays by proton–proton interactions of wind accelerated protons and shocked matter is negligible when compared with emission from IC scattering. For this reason, we do not compute the luminosity produced by this emission channel. Besides that, the synchrotron and IC emission from $e^{\pm}$ secondaries of these proton–proton interactions will be much smaller than that from primary electrons.

6 FLARING EMISSION FROM A WOLF–RAYET STAR

WR stars evolve from OB-type stars. Typically, WR stars have masses $\sim$10–25 M$_\odot$, and strong mass-loss rates, $\sim 10^{-4}$ M$_\odot$ yr^{-1}. They are very luminous, $L_{\rm WR} \sim 10^{39}$ erg s^{-1}, reaching photospheric radius as large as $\sim 10^2$ R$_\odot$ in the most powerful cases (Crowther 2007). Since WR stars are scarce, it is not expected to find large populations of WR stars in the inner region of AGN, we will consider here the situation of a single WR star interacting with the AGN jet. The winds of WR stars are so powerful that can balance the ram pressure of a jet with $L_{\rm j0} = 1.2 \times 10^{42}$ erg s^{-1} at any z, since $z_\star \sim 0.74\,(L_{\rm j0}/10^{42}\ {\rm erg\ s^{-1}})^{1/2} z_0$ for the properties of the WR star listed in Table 3.

In order to compare the spectrum produced by a WR star and by standard massive (OB) stars as was shown in Section 5, we assume that the WR penetrates the jet at $z = 1$ pc in the case with $L_{\rm j0} = 1.2 \times 10^{42}$, 1.2×10^{44} and 1.2×10^{46} erg s^{-1}. Being $\dot{M}_{\rm WR}/\dot{M}_\star = 100$, the stagnation point of the WR wind is located at $R_{\rm sp,\,wr} \sim 10 R_{\rm sp}$. Thus, the available luminosity to accelerate particles

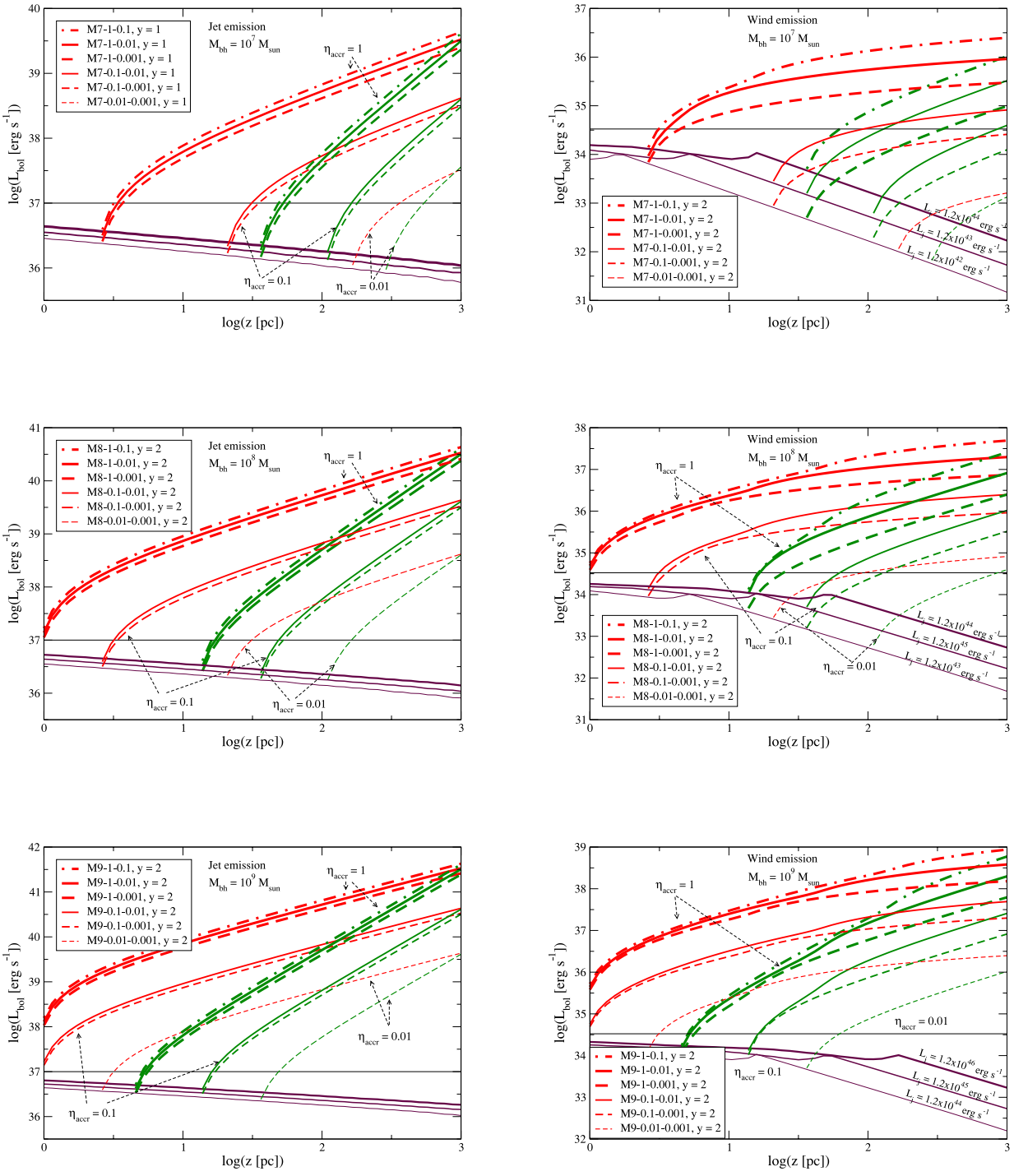

Figure 7. Bolometric luminosities (maroon solid lines) in the jet (left) and in the wind (right), produced by the interaction of only one star along the whole jet: from 1 pc to 1 kpc. The thickness of maroon lines is increased from low to large values of L_j, as is indicated in the right-hand panel. The bolometric luminosity of many stars up to a certain z is also presented. Cases with $M_{bh} = 10^7$ (top), 10^8 (middle) and 10^9 $M_\odot$ (bottom) are shown. In each plot, the results of the two spatial distribution models ($y = 1$ – green lines – and 2 – red lines) are presented. The thickness of green and red lines is increased from low to large values of η_{accr}. The black line indicates the value of L_{jbs} (left) and L_{wbs} (right).

in the shocks produced by the interaction of the WR is ∼100 times larger than in the case of an OB star. In Fig. 8 we show the synchrotron and IC emission produced in the jet and in the wind. Note that the IC emission from the wind reaches similar levels to the IC emission from the jet, on the contrary to the case of an OB star, where the IC jet emission in the case of 1.2×10^{46} erg s^{-1} is ∼100 times smaller in the wind than in the jet. This is a consequence of the different energy breaks in the electrons energy distribution. Comparing the curves that correspond to $z = 1$ pc in Fig. 6 with Fig. 8 we can appreciate that the shape of synchrotron and IC spectrum in the jet is different for the case of an OB star and a WR, where in the former case the break energy produced by the advection escape

Table 3. Parameters of the WR star considered in this work.

Description	Value
Mass-loss rate	$\dot{M}_{\rm WR} = 10^{-4}\ {\rm M}_\odot\ {\rm yr}^{-1}$
Wind terminal velocity	$v_{\rm WR} = 3000\ {\rm km\ s}^{-1}$
Luminosity	$L_{\rm WR} = 10^{39}\ {\rm erg\ s}^{-1}$
Surface temperature	$T_{\rm WR} = 3 \times 10^4\ {\rm K}$

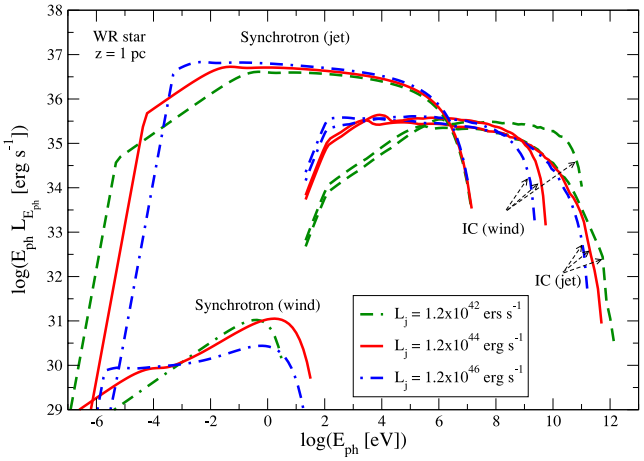

Figure 8. Synchrotron radiation and IC scattering produced in the jet and in the wind by the interaction of a WR star with a jet of $L_{\rm j0} = 1.2 \times 10^{42}$ (green dashed line), 1.2×10^{44} (red solid line) and 1.2×10^{46} erg s^{-1} (blue dot–dashed line) at $z = 1$ pc. The main contributions to the SED are synchrotron radiation in the jet and IC scattering in the jet and in the wind. However, synchrotron emission produced in the wind is also plotted in order to compare this figure with Fig. 6.

to the radiation-dominated regime is at higher energies than in the latter. Finally, the emission level produced by a WR (both in the wind and in the jet) is larger than the one produced by an OB star (both interacting with the jet at the same z).

The radiation produced by a WR interacting occasionally with a jet will be transient with a time-scale similar to the jet crossing time, unlike the steady emission produced by a population of stars, described in the next section. We remark that if the star diffusion time were short enough to allow a massive star to reach the vicinity of the SMBH in the WR stage, the luminosity due to the jet–WR interaction would be significantly higher than obtain for an interaction distance of 1 pc. It is noteworthy that one or few WR may be recurrently present within the jet and close to its base, where radiative cooling is still dominant, adding up to the contribution of the many star persistent emission. In fact, WR could be important contributors of their own to the non-thermal output of misaligned AGN jets.

7 STEADY EMISSION FROM A POPULATION OF MASSIVE STARS

In order to study the emission produced by many massive stars, we assume within the jet a stellar population as the one described in Section 2. As shown in Section 5, the emission produced at small values of z is higher than the emission produced at larger z, as a consequence of the dilution of the target fields with z. This effect is balanced by the fact that, at $z > z_1$, the number of stars interacting with the jet is >1 and the emission produced by all of them increase $\propto z^2$ and $\propto z$, for the cases with $y = 1$ and 2, respectively. We calculate the emission produced by each of the $N_{\star {\rm j}}$ stars at a certain z, and then integrate along z all the contributions, obtaining the SEDs shown in Fig. 9, for different values of $M_{\rm bh}$ and $L_{\rm j}$. Note that the features of these SEDs are similar to the SED produced by only one star located at a relatively large value of z (see Fig. 6), where advection losses become dominant. In the range $z > 1$ pc, $R_{\rm sp}$ is large enough to suppress the effect of photon–photon absorption. In the case of $L_{\rm j} = 1.2 \times 10^{46}$ erg s^{-1}, the synchrotron and IC emission achieve levels of $\gtrsim 5 \times 10^{39}$ erg s^{-1} in hard X-rays and $\sim 10^{38}$ erg s^{-1} in gamma-rays, respectively.

In Fig. 7, the bolometric luminosities (synchrotron + IC) at different z and for a variety of stellar distributions are shown. In Section 5 we have commented about the non-thermal bolometric luminosity ($L_z^{\rm j}$ and $L_z^{\rm w}$) produced by the interaction of only one star with the jet at different z, from 1 pc to 1 kpc (maroon solid lines). However, at $z \gtrsim z_1$ there are more than one star every time into the jet, and the non-thermal luminosity produced by all the stars into the jet at different z is also plotted in Fig. 7. In each panel we show the bolometric luminosity produced by the different stellar populations considered in the present study. Note that on the one hand, in the most powerful case (M9-1-0.1) the total bolometric luminosity produced in the jet and in the wind is $\sim 5 \times 10^{41}$ and $\sim 10^{39}$ erg s^{-1} ($y = 2$), respectively. On the other hand, in cases with low density of massive stars, the luminosity produced by the cumulative effect of all stars into the jet can be lower than the luminosity produced by only one star interacting with the jet close to z_0 if the star formed at $z \gtrsim r_{\rm t}$ and migrated close to the jet base.

Considered the $\dot{M}_\star$–$\dot{M}_{\rm bh}$ relation given by Satyapal et al. (2005), the density of massive stars results $\propto (\eta_{\rm accr} M_{\rm bh})^{0.89}$. Thus, sources with $M_{\rm bh} = 10^8$–10^9 M$_\odot$ and $\eta_{\rm accr} \sim$ 1–0.1 are likely to be detected at gamma-rays by *Fermi* with a deep enough (pointed) exposure or after some years of observation in the survey mode. In the case of stellar populations around a SMBH with $M_{\rm bh} = 10^7$ M$_\odot$, the gamma-ray emission produced cannot be detected by *Fermi* in any case, and the same occurs for $M_{\rm bh} = 10^8$ M$_\odot$ and $\eta_{\rm accr} \sim 0.01$ (under the assumed $\eta_{\rm B}$ and $\eta_{\rm nt}$). The most interesting case is that of a high accretion rate $\eta_{\rm accr} \sim 1$ and $M_{\rm bh} = 10^9$ M$_\odot$ yr^{-1}, whose emission can be detected in the case of luminous ($L_{\rm j} \sim 10^{46}$ erg s^{-1}) and close sources (such as M87). Less luminous sources may also be detected in the near future by the Cherenkov Telescope Array (CTA).

In the case of a population of massive stars (continuously) interacting with the jet, the produced emission will be steady and produced in a large part of the jet volume, from z_1 to z_2, on scales of $\sim$kpc.

8 DISCUSSION AND SUMMARY

In this work we have studied the interaction of massive stars with relativistic jets of AGN, focusing on the production of gamma-rays from particles accelerated in the double bow-shock structure formed around the stars as a consequence of the jet/stellar wind interaction. We calculated the energy distribution of electrons accelerated in the jet and in the wind, and the subsequent non-thermal emission from these relativistic particles. In the jet and wind shocked regions, the most relevant radiative processes are synchrotron emission and IC scattering of stellar photons. In the wind shocked region, the gamma-ray luminosity from proton–proton interactions in the stellar wind is well below the IC one.

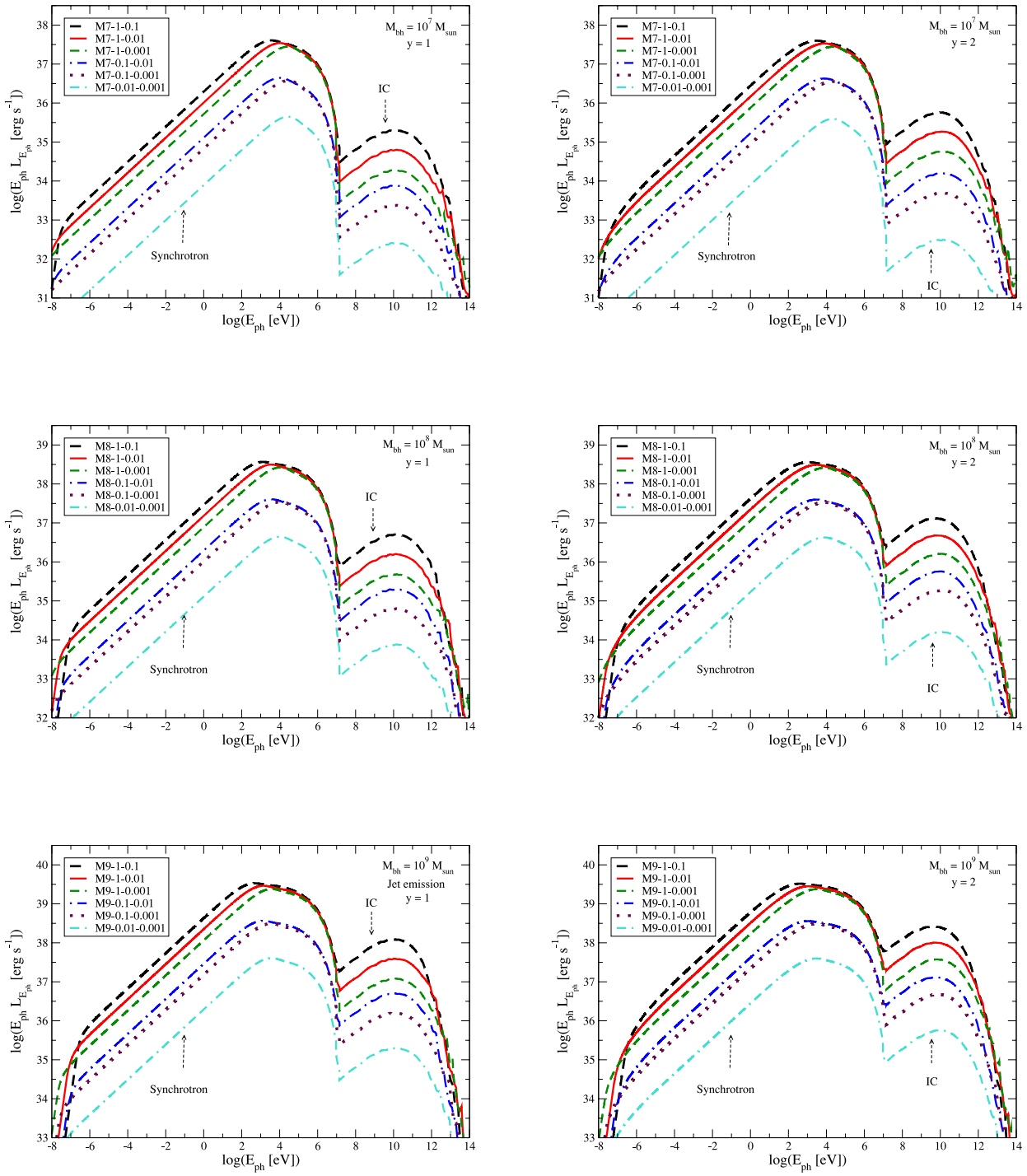

Figure 9. SED of the emission up to $z = 1$ kpc produced by $N_{\star,\mathrm{j}}$ stars inside the jet. The main contributions to the SED are synchrotron radiation and IC scattering; proton–proton interactions are not relevant. Left-hand panel is for the case of $y = 1$, and the right one for $y = 2$. Cases with $M_{\mathrm{bh}} = 10^7$ (top), 10^8 (middle) and 10^9 $\mathrm{M}_\odot$ (bottom) are shown.

We have studied two scenarios: the interaction of a WR star at 1 pc; and the interaction of a population of massive stars with the whole jet. The properties of the emission generated in the downstream region of the bow shocks change with z. On the one hand, the target densities for radiative interactions decrease as z^{-2}. On the other hand, the time of the non-thermal particles inside the emitter is $\propto R_{\mathrm{sp}} \propto z$, and the number of stars per jet length unit $\mathrm{d}N_{\star,\mathrm{j}}/\mathrm{d}z \propto z$ and z^2, for cases with $y = 2$ and 1, respectively. Therefore, for a population of stars, the last two effects soften the emission drop with z.

The interaction of only one star with the jet can produce significant amounts of high-energy emission only if the interaction height is below the z at which advection escape dominates the whole particle population. Also, σ_{sp} should be a significant fraction of σ_{j}. In this context, we have considered the interaction of a powerful WR star at $z = 1$ pc. The emission produced by IC scattering achieves values

as high as $\gtrsim 10^{36}$ erg s^{-1} (considering the contribution of the wind and jet in Fig. 8) in the *Fermi* range. Such an event would not last long though, about $R_{\rm j}/v_\star \sim 300\,(R_{\rm j}/3\times10^{17}\,{\rm cm})\,(10^9\,{\rm cm\,s^{-1}}/v_\star)^{-1}$ yr. The emission level could be detectable by *Fermi* only for very nearby sources, like Centaurus A (located at a distance $d\sim4$ Mpc). The interaction of few WR stars interacting with jets in more distant sources like M87 ($d\sim16$ Mpc) could be detectable by the forthcoming CTA. The interaction of a star even more powerful than a WR, like a luminous blue variable, may provide $R_{\rm sp}\sim R_{\rm j}$, making available the whole jet luminosity budget for particle acceleration.

In the middle/end part of the jet, the interaction of many massive stars can also produce a significant amount of gamma-rays. The resulting SED integrated along the whole jet strongly depends on the number of stars inside it. We have considered a Salpeter initial mass function of stars distributed following a power-law spatial distribution (equation 1). In the case of $M_{\rm bh}=10^9\,{\rm M}_\odot$, and high accretion rates ($\eta_{\rm accr}=1$), gamma-ray luminosities $\sim10^{38}$ and 5×10^{38} erg s^{-1}, for $y=1$ and 2, respectively, may be achieved (see Fig. 9). However, note that few WR inside the jet could actually dominate over the whole main-sequence OB star population.

Although jet/star interactions are very sporadic near the base of the jet, we note that at $z<1$ pc, clouds from the BLR can also interact with the jet, leading to significant gamma-ray radiation (Araudo et al. 2010). The produced emission in BLR clouds interacting with jets has a stronger dependence on $L_{\rm j}$ than in the case of stellar winds, because clouds do not have winds and their cross-section does not get adjusted to ram pressure balance. Thus, jet/BLR cloud interactions could be more relevant in sources like FR II galaxies.

An interesting (similar) scenario is the interaction of a star-forming region (SFR) with the jet. There is evidence that SFRs are located in the torus of some AGN (starburst galaxies), at distances $\sim$100 pc from the nucleus. In addition, hints of SFRs located in the nuclear region of AGN are also found in galaxies with IR nuclear excess. These galaxies are called nuclear starburst galaxies. The number of OB-type stars in SFRs can be as high as $\sim10^4$, distributed in a small volume of $\sim10\,{\rm pc}^3$. Then, if one of these compact SFRs interact with the jet at $z\sim10$ pc, the total luminosity could reach detectable levels, with the resulting radiation presenting rich and complex features. Furthermore, the jet passing through the intracloud rich medium can have interesting consequences in the SFR evolution. This scenario will be analysed in detail in a following paper.

It is noteworthy that, for $\eta_{\rm accr}\lesssim1$, one expects $\sim10^4$ massive stars up to $\sim$1 kpc. Moreover, as shown in Section 3.1, the shocked stellar wind will efficiently mix with the jet. Assuming an average $\dot{M}_{\rm w}\sim10^{-6}\,{\rm M}_\odot\,{\rm yr}^{-1}$, one can estimate the power required to accelerate this mass to the jet Lorentz factor, $\Gamma\,\dot{M}_{\rm w}\,c^2\sim6\times10^{44}\,{\rm erg\,s^{-1}}$. Despite this is just an order of magnitude estimate, this power tells us that the dynamics of jets with similar or smaller power, i.e. $\lesssim10^{45}$ erg s^{-1}, will be significantly affected by wind mass loading (e.g. Hubbard & Blackman 2006). Therefore, early-type stars, as low-mass ones (Komissarov 1994), cannot be neglected when studying jet propagation and evolution in galaxies with moderately high star formation. Even for $\eta_{\rm accr}\sim0.01$, jets with $L_{\rm j}\sim10^{42}$ erg s^{-1} may be strongly affected by the entrainment of wind material (see also the discussion on mass load in Bosch-Ramon, Perucho & Barkov 2012).

Finally, we remark that since jet–star emission should be rather isotropic (as in all the cases of jet–obstacle interactions), it would be masked by jet beamed emission in blazar sources. Misaligned sources however do not display significant beaming, and for those cases jet–star interactions may be a dominant gamma-ray production mechanism. In the context of AGN unification (e.g. Urry & Padovani 1995), the number of non-blazar AGN should be much larger than that of blazars with the same $L_{\rm j}$. Close and powerful sources could be detectable by deep enough observations of the *Fermi* gamma-ray satellite. After few year exposure, a significant signal from jet–star interactions could be found, and their detection would shed light not only on the jet properties but also on the stellar populations in the vicinity of AGN. The same applies to stars with powerful winds penetrating the jet at its innermost regions, which may be seen as occasional, transient month-scale gamma-ray events.

ACKNOWLEDGEMENTS

The authors thank the referee for valuable comments that improved the paper. We thank G. Bruzual, J. Cantó, S. Cellone, A. Raga and L. F. Rodríguez for contributing to this work with useful suggestions and comments. ATA thanks M. Orellana and P. Santamaría for help with numerical calculations. ATA is very grateful for the hospitality of the Dublin Institute of Advanced Studies (DIAS) where this project started. This project is financially supported by CONACyT, Mexico and PAPIIT, UNAM; PIP 0078/2010 from CONICET and PICT 627/2008 and 848/2007 of Agencia de Promoción Científica y Técnica, Argentina. GER and VB-R acknowledge support by the former Ministerio de Ciencia e Innovación (Spain) under grant AYA 2010-21782-C03-01. VB-R also acknowledges support from grant FPA2010-22056-C06-02 and from MINECO through a Ramón y Cajal fellowship. This research has been supported by the Marie Curie Career Integration Grant 321520.

REFERENCES

Abdo A. A. et al., 2010, ApJ, 720, 912
Achterberg A., Gallant Y. A., Kirk J. G., Guthmann A. W., 2001, MNRAS, 328, 393
Aharonian F. A., 2002, MNRAS, 332, 215
Alexander T., 2005, Phys. Rep., 419, 65
Araudo A. T., Bosch-Ramon V., Romero G. E., 2009, A&A, 503, 673
Araudo A. T., Bosch-Ramon V., Romero G. E., 2010, A&A, 522, A97
Barkov M. V., Aharonian F. A., Bosch-Ramon V., 2010, ApJ, 724, 1517
Barkov M. V., Aharonian F. A., Bogovalov S. V., Kelner S. R., Khangulyan D., 2012, ApJ, 749, 119
Bednarek W., Protheroe R. J., 1997, MNRAS, 287, L9
Begelman M. C., Blandford R. D., Rees M. J., 1984, Rev. Modern Phys., 56, 255
Bisnovatyi-Kogan G. S., Blinnikov S. I., 1977, A&A, 59, 111
Blandford R. D., Konigl A., 1979, ApJ, 232, 34
Blumenthal G. R., Gould R. J., 1970, Rev. Modern Phys., 42, 237
Bosch-Ramon V., Perucho M., Barkov M. V., 2012, A&A, 539, A69
Böttcher M., 2007, Ap&SS, 309, 95
Crowther P. A., 2007, ARA&A, 45, 177
Crowther P., 2012, Astron. Geophys., 53, 040000
Dar A., Laor A., 1997, ApJ, 478, L5
Drury L. O., 1983, Rep. Progress Phys., 46, 973
Ekström S. et al., 2012, A&A, 537, A146
Ghisellini G., Maraschi L., Treves A., 1985, A&A, 146, 204
Ginzburg V. L., Syrovatskii S. I., 1964, The Origin of Cosmic Rays. Macmillan, New York
Hopkins P. F., Quataert E., 2010, MNRAS, 407, 1529
Hubbard A., Blackman E. G., 2006, MNRAS, 371, 1717
Ito H., Kino M., Kawakatu N., Isobe N., Yamada S., 2008, ApJ, 685, 828
Junor W., Biretta J. A., Livio M., 1999, Nat, 401, 891
Kelner S. R., Aharonian F. A., Bugayov V. V., 2006, Phys. Rev. D, 74, 034018

Khangulyan D. V., Barkov M. V., Bosch-Ramon V., Aharonian F. A., Dorodnitsyn A. V., 2013, ApJ, 774, 113
Komissarov S. S., 1994, MNRAS, 269, 394
Komissarov S. S., Barkov M. V., Vlahakis N., Königl A., 2007, MNRAS, 380, 51
Kroupa P., 2001, MNRAS, 322, 231
Lamers H. J. G. L. M., Cassinelli J. P., 1999, Introduction to Stellar Winds. Cambridge Univ. Press, Cambridge
Leitherer C., Heckman T. M., 1995, ApJS, 96, 9
López-Sánchez Á. R., 2010, A&A, 521, A63
Mannheim K., 1993, A&A, 269, 67
Mor R., Netzer H., Trakhtenbrot B., Shemmer O., Lira P., 2012, ApJ, 749, L25
Mücke A., Protheroe R. J., 2001, Astropart. Phys., 15, 121
Murphy B. W., Cohn H. N., Durisen R. H., 1991, ApJ, 370, 60
Rees M. J., 1978, MNRAS, 184, 61P
Reynoso M. M., Medina M. C., Romero G. E., 2011, A&A, 531, A30
Romero G. E., Reynoso M. M., 2011, J. Astrophys. Astron., 32, 19
Salpeter E. E., 1955, ApJ, 121, 161
Sanders D. B., Mirabel I. F., 1996, ARA&A, 34, 749
Satyapal S., Dudik R. P., O'Halloran B., Gliozzi M., 2005, ApJ, 633, 86
Schödel R., Merritt D., Eckart A., 2009, A&A, 502, 91
Shakura N. I., Sunyaev R. A., 1973, A&A, 24, 337
Urry C. M., Padovani P., 1995, PASP, 107, 803
Usov V. V., Melrose D. B., 1992, ApJ, 395, 575
Zhao H., 1997, MNRAS, 287, 525

This paper has been typeset from a TEX/LATEX file prepared by the author.